Applied Catalysis B: Environmental 237 (2018) 32–42

Contents lists available at ScienceDirect

Applied Catalysis B: Environmental

journal homepage: www.elsevier.com/locate/apcatb

N-Annulated perylene-based organic dyes sensitized graphitic carbon nitride to form an amide bond for efficient photocatalytic hydrogen production under visible-light irradiation

Fengtao Yu[a,1], Zhiqiang Wang[b,1], Shicong Zhang[a], Kang Yun[a], Haonan Ye[a], Xueqing Gong[b,*], Jianli Hua[a,*], He Tian[a]

[a] Key Laboratory for Advanced Materials, Institute of Fine Chemicals and School of Chemistry and Molecular Engineering, East China University of Science and Technology, 130 Meilong Road, Shanghai, 200237, PR China

[b] Key Laboratory for Advanced Materials, Centre for Computational Chemistry and Research Institute of Industrial Catalysis, School of Chemistry and Molecular Engineering, East China University of Science and Technology, Shanghai 200237, PR China

ARTICLE INFO

Keywords:
N-annulated perylene
graphitic carbon nitride
amide bond
photocatalytic
H2 evolution

ABSTRACT

In this work, two new N-annulated perylene-based organic sensitizers (**PY-1** and **PY-2**) have been developed for dye-sensitized graphitic carbon nitride (g-C_3N_4) to remarkably enhance photocatalytic hydrogen production under visible-light irradiation (420 nm ≤ λ ≤ 780 nm). The results showed that the H_2 production rates of the **PY-1**/g-C_3N_4/Pt and **PY-2**/g-C_3N_4/Pt were up to 5508.1 μmol h^{-1} g^{-1} and 11,855.4 μmol h^{-1} g^{-1}, respectively, which were 8.98 and 19.3 times higher than that of the g-C_3N_4/Pt, respectively. Specifically, an impressive record apparent quantum efficiency (AQY) of 27.16% for **PY-2**/g-C_3N_4/Pt system was achieved at λ = 550 nm monochromatic light irradiation. Moreover, the formation of amide bonds between dye molecules and g-C_3N_4 was firstly confirmed by FTIR spectrum and theoretical calculation. The amide bonds provided the electron transfer channels to significantly improve interface charge transfer and separation, thus resulting in a more efficient hydrogen production. More importantly, **PY-1**/g-C_3N_4/Pt and **PY-2**/g-C_3N_4/Pt displayed good stability under long-term irradiation and was favorable and significant for practical application. Our work indicated that dye sensitized g-C_3N_4 to form an amide bond is a promising strategy to realize the effective conversion of solar energy to hydrogen energy through molecular engineering.

1. Introduction

With the further deterioration of environmental contamination and energy crisis, seeking environmentally and friendly renewable energy has been imminent. In the past decades, hydrogen energy production has been widely concerned, because of its carbon-free and high-energy capacity [1]. One promising strategy for hydrogen production is artificial photosynthesis with semiconductor-based photocatalysts under sunlight irradiation, and the biggest challenge is how to effectively use the visible-light since it accounts for 47% of sunlight [2–5]. So, much effort has been carried out to extend the visible-light response range of the semiconductor-based photocatalysts, such as doping with nonmetal [6], construction of heterojunctions [7,8], and organic dyes sensitization [9–11].

Recently, graphitic carbon nitride (g-C_3N_4), a novel metal-free polymer semiconductor with a graphite-like sp^2-bonded C–N structure, has attracted numerous attention, because of its unique planar structure, outstanding physicochemical properties and appropriate energy band positions for the photocatalytic water reduction and oxidation processes [12–19]. Generally, the photoactivity of pure g-C_3N_4 is relatively unsatisfied due to its poor visible-light beyond 460 nm, high recombination rate of the photogenerated carriers as well as relatively small Brunauer-Emmett-Teller (BET) surface area (normally below 10 m^2 g^{-1}) [20–23]. Therefore, considerable effort has been devoted to increase the photocatalytic performance of g-C_3N_4, such as coupling with other functional semiconductors to construct heterojunction structures, [24–26] modulating the shape and morphology [27,28], and protonating and polymerizating the pristine g-C_3N_4 [29]. However, these methods mentioned above are rather complex and time-consuming, which greatly limits the development of g-C_3N_4-based photocatalysts for the large-scale applications. Hence, it is highly desirable to develop a rapid, low-cost, and convenient method to construct highly

* Corresponding authors.
E-mail addresses: xgong@ecust.edu.cn (X. Gong), jlhua@ecust.edu.cn (J. Hua).
[1] Authors are equal to contribution.

https://doi.org/10.1016/j.apcatb.2018.05.045
Received 6 March 2018; Received in revised form 14 May 2018; Accepted 15 May 2018
Available online 23 May 2018

photocatalytic activity g-C_3N_4-based hybrid photocatalytic materials in order to meet the practical application.

Among the various strategies for extending the visible-light response range, dye sensitization was considered to be the most effective [11]. Up to now, dye-sensitized g-C_3N_4 for photocatalytic application has received wide attention because the photocatalytic activity was greatly improved with spectral response region above 460 nm [30]. Currently, magnesium phthalocyanine and xanthene dyes were widely used for dye-sensitized g-C_3N_4 to improve the photocatalytic activity by broadening the visible-light response region [31–33]. Peng and co-workers also synthesized **LI-4**/g-C_3N_4 composite photocatalyst, which was active for photocatalytic H_2 production under visible-light [34], but its visible-light response range limited to 400–600 nm, resulting in relatively low hydrogen production activity. It was proved that the spectral response ability of photocatalyst has a great influence on the hydrogen production activity [35]. Therefore, it is important to optimize the dye structures with strong interface interaction and wide spectral response for sensitizing g-C_3N_4 to improve photocatalytic activity.

N-annulated perylene (NP) derivatives, have received considerable attention due to their excellent optical and physical properties such as high molar extinction coefficient, high fluorescence quantum and tunable energy band gap [36]. The recent breakthrough of NP derivatives as sensitizers in DSSCs makes them also a practical sensitizer in dye-sensitized photocatalytic system which is somewhat similar to the photovoltaic devices, in terms of the photogenerated electron transfer processes [37–39]. In addition, primary requirement for efficient H_2 production by dye sensitization is the strong interaction between molecules and g-C_3N_4, because the dye excited state is typically too short-lived to allow for diffusion of the dye molecule to g-C_3N_4. To date, cyanoacrylic acid group has been widely used in DSSCs and dye-sensitized photocatalytic system for anchoring dye molecules to the TiO_2 surface with good electron injection efficiency [40–42]. However, it is rarely reported for graphite carbonitride systems.

Herein, two new NP metal-free organic sensitizers termed **PY-1** and **PY-2** (Scheme 1) with different π-linker lengths (thiophene or cyclopentadithiophene thiophene as the π-linker) and carboxylic acid as anchoring group were designed and synthesized. The performance of dye-sensitized g-C_3N_4 for H_2 production under visible- light irradiation (420 nm ≤ λ ≤ 780 nm) were tested. It was found that the H_2 evolution rates of the **PY-1**/g-C_3N_4/Pt and **PY-2**/g-C_3N_4/Pt under visible-light irradiation with ascorbic acid (AA) as the sacrificial electron donor were 5508.1 μmol h^{-1} g^{-1} and 11,855.4 μmol h^{-1} g^{-1}, respectively, which were 8.98 and 19.3 times higher than that of the g-C_3N_4/Pt, respectively. Importantly, an AQY of 27.16% at λ = 550 nm were achieved in **PY-2**/g-C_3N_4/Pt system. In order to further study the photogenerated electron transfer process between dye and g-C_3N_4 on both thermodynamics and dynamics aspects, spin-unrestricted density functional theory (DFT) calculations and a series of photoelectrochemical measurements were carried out. In addition, the possible mechanism for the photocatalytic H_2 production process under visible-light irradiation was put forwarded.

2. Experimental section

2.1. Materials and measurements

The starting materials of 3-bromo-1-(2-ethylhexyl)-10-(4-((2-ethylhexyl)oxy)

phenyl)-1H-phenanthro[1,10,9,8-cdefg]carbazole and intermediate 5-(7-bromo- benzo[c][1,2,5]thiadiazol-4-yl)thiophene-2-carbaldehyde were synthesized according to our previous paper [53,54]. All other solvents and chemicals used for synthesis were from commercial sources and used without further purification unless otherwise specified. Glassware was dried in oven prior to use. All chemical reactions were carried out under an inert argon atmosphere.

^1H and ^{13}C NMR spectra were obtained in deuterated solvents on Bruker AM-400 MHz usingtetramethylsilane (*TMS*) as an internal standard. High-resolution mass spectra (HRMS) measurements were performed using a Waters LCT Premier XE spectrometer.

2.2. Photophysical measurements

The UV–vis absorption spectra of dyes in solution and adsorbed on TiO_2 films and UV–vis diffuse reflectance spectroscopywere (*DRS*) of composites were measured with a Varian Cary 500 spectrophotometer. Photoluminescence (PL) spectrum was obtained on a Hitachi F-4500 fluorescence spectrophotometer at RT. Time-resolved fluorescence spectra (TRFS) were obtained on an Edinburgh FES 920 with an excitation wavelength of 377 nm. The Fourier transform infrared (FTIR) spectra was recorded on NICOLET 380 spectrometer using a standard KBr pellet technique in the frequency range of 4000-400 cm^{-1}. Powder X-ray diffraction (XRD) patterns was obtained on a Bruker D8-Advance X-ray diffractometer with monochromatized Cu Kα radiation (λ = 1.5418 Å).

2.3. Electrochemical measurements

The redox behaviors and stability of sensitizer molecules were analyzed by cyclic voltammetry (CV) in DCM solutions without

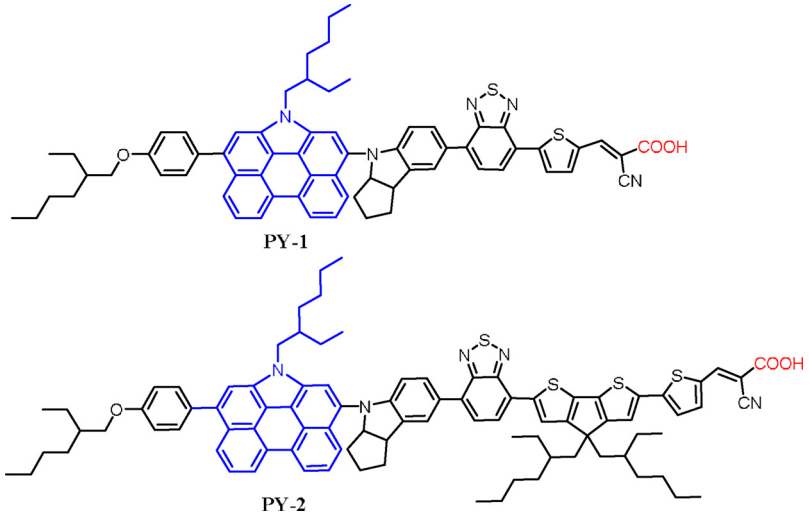

Scheme 1. Molecular structures of the dyes **PY-1** and **PY-2**.

deoxidization. The CV curves were measured by a CHI660C electrochemical workstation in a normal three-electrode cell which using glassy carbon as the working electrode, Pt wire as counter electrode and Ag/AgCl electrode as the reference electrode. The experiments were carried out in DCM solutions with 0.1 M tetra-n-butylammonium hexafluorophosphate ($TBAPF_6$) as the supporting electrolyte at a scan rate of 100 mV s^{-1}. The ferrocenium/ferrocene (Fc/Fc^+) redox couple was used as an external potential reference. A Zahner IM6e Impedance Analyzer (ZAHNER-Elektrik GmbH & CoKG, Kronach, Germany) was employed to carry out electrochemical impedance spectroscopy of the DSSCs. The frequency range was 0.1 Hz to 100 kHz and the applied bias was from -0.45 V to -0.8 V with about 50 mV progressive increase under dark conditions. The magnitude of the alternating signal was 5 mV, and the spectra were characterized with Z-View software. The linear scan voltammetry (LSV), transient photocurrent responses (I-t) and electrochemical impedance spectra (EIS) of dye-loaded g-C_3N_4 films electrode were measured by using a CHI660C electrochemical workstation in a three-electrode system. The as-prepared g-C_3N_4 films electrodes served as working electrodes, a Pt flake was used as the counter electrode and Ag/AgCl as the reference electrode. An aqueous solution of 0.5 M Na_2SO_4 was used as the supporting electrolyte and a 300 W Xe-lamp served as the light source. The photocurrent intensity of g-C_3N_4 films electrodes were measured at 0.3 V vs Ag/AgCl with the light on and off. EIS was determined over the frequency range of 10^2-10^6 Hz with an ac amplitude of 10 mV at the open circuit voltage under room-light illumination.

2.4. Synthesis of g-C_3N_4 and dye/g-C_3N_4/Pt composites

Graphitic carbon nitride (g-C_3N_4) were prepared according to published procedures with some modifications [47,48]. Typically, 15 g of urea was put in a ceramic container with a cover and heated under static air at 550 ℃ for 2 h with a ramping rate of 5 ℃ min^{-1}. The resultant light-yellow powder was collected for use without further treatment. To improve photocatalytic activity, quantitative Pt metal was deposited onto g-C_3N_4 powder by photochemical reduction method according to literature [47]. Briefly, g-C_3N_4 powder (600 mg) and $H_2PtCl_6{\cdot}6H_2O$ (1.6 mL, 1 g/L) were added to a mixture methanol aqueous (400 mL, V/V = 3:1) in a 500 mL beaker, then the resulting solution was irradiated with a Xe lamp (300 W) for 5 h. Finally, the resultant 1.0 wt% g-C_3N_4/Pt composite was obtained by centrifugation at 4000 rpm, washed 3 times with distilled water and then dried under vacuum at 80 ℃ for 12 h in darkness. Then, 1.0 wt% g-C_3N_4/Pt (100 mg) composite was immersed in a THF/Ethanol mixture solution containing dye sensitizers (10 mL V: V = 1:1), then the resulting solution was kept stirring at RT in the dark for 24 h. Finally, the resultant dye/g-C_3N_4/Pt composites was obtained by centrifugation at 4000 rpm, rinsed with distilled water for 3 times and then dried under vacuum at 80 ℃ for 12 h in darkness. It was used for hydrogen production reaction without further treatment.

2.5. Photocatalytic activity measurement

The photocatalytic H_2 generation experiments were operated in a glass gas-closed-circulation system under irradiation with a 300-W xenon lamp (CEL-HXBF 300). The quantitative dye/g-C_3N_4/Pt catalyst was suspended in 50 mL (containing 5 g ascorbic acid (AA)) aqueous. It was then air sealed with a rubber septum. Before light irradiation, the dissolved air must be thoroughly removed by vacuum pump. And then the aqueous suspension was irradiated from the top using a 300 W xenon lamp jointing a cut-off filter to obtain visible-light irradiation (420 nm ≤ λ ≤ 780 nm). The reaction mixture was kept under constant stirring using a magnetic stirring bar during the course of irradiation and the amount of H_2 gas was detected with a gas chromatograph (GC 2060, TCD detector and Ar carrier). The TON for H_2 evolution with respect to the sensitizer and the apparent quantum yield (AQY) at monochromatic light irradiation were estimated as the following equation.

$$TON = \frac{2\times \text{number of evolved} H_2 \text{molecules}}{\text{number of dye molecules adsorbed}} \quad (1)$$

$$AQY\,(\%) = \frac{2\times \text{number of evolved} H_2 \text{molecules}}{\text{number of incident photons}} \times 100\% = \frac{2 \times CN_A}{Pt\lambda/hc} \times 100\% \quad (2)$$

2.6. DFT calculation methods

Spin-unrestricted density functional theory (DFT) calculations were performed using the Gaussian 09 program package [55]. All structures and the frontier molecular orbitals were optimized without symmetry constrains at the B3LYP/6-31G* level [56]. The adsorption energy (E_{ads}) was calculated as follows:

$$E_{ads} = -(E_{total} - E_{substrate} - E_{gas\text{-}phase\ adsorbate})$$

where E_{total} is the calculated total energy of the adsorption system, $E_{substrate}$ is the energy of the clean substrate (g-C_3N_4) and $E_{gas\text{-}phase\ adsorbate}$ is the energy of the gas-phase molecule (**PY-1** and **PY-2**). The wave functions of the frontier molecular orbitals are shown in Figure S1 in ESI. In order to form the amide bond (−CO—NH—), we designed the g-C_3N_4 model according to the literature [57] is listed as follows.

Model molecule for g-C_3N_4:

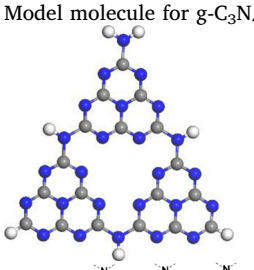

for

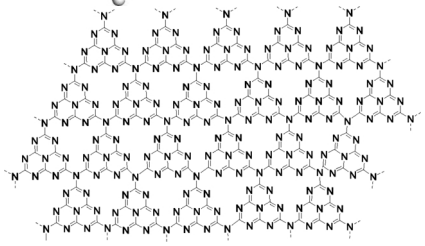

Model molecule for **PY-1** :

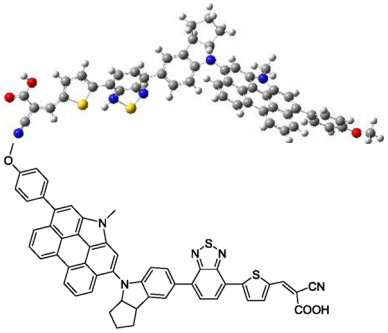

for

Model molecule for **PY-2**:

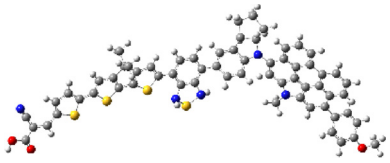

for 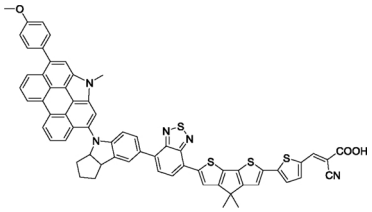

Model molecule for **PY-1**/g-C_3N_4:

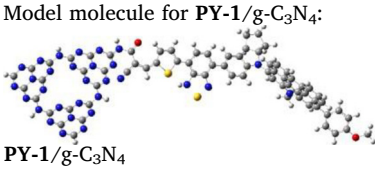

for **PY-1**/g-C_3N_4

Model molecule for **PY-2**/g-C_3N_4:

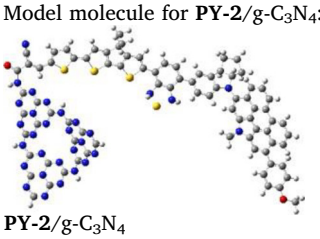

for **PY-2**/g-C_3N_4

As calculated at the DFT Gaussian B3LYP/6-31G* level, the HOMO and LUMO positions of **PY-1**, **PY-2**, g-C_3N_4, **PY-1**/g-C_3N_4 and **PY-2**/g-C_3N_4 were listed as follows (vs vacuum):

PY-1: HOMO = -4.88 eV; LUMO = -2.72 eV; E_g = 2.16 eV;

PY-2: HOMO = -4.58 eV; LUMO = -2.69 eV; E_g = 1.89 eV;

g-C_3N_4: HOMO = -6.50 eV; LUMO = -2.87 eV; E_g = 3.63 eV;

PY-1/g-C_3N_4: HOMO = -4.97 eV; LUMO = -3.31 eV; E_g = 2.16 eV;

PY-2/g-C_3N_4: HOMO = -4.66 eV; LUMO = -3.35 eV; E_g = 2.16 eV;

3. Results and discussion

3.1. Molecular design and synthesis

The design strategy was to construct organic dyes with high molar extinction coefficients (ε) and broad absorption spectra to improve visible-light capture capability in dye-sensitized g-C_3N_4. Thus, 1,2,3,3a,4,8b-hexahydrocyclopenta[b]indole functionalized NP with a strong electron-donating ability was introduced as the donor, and benzothiadiazole unit was also used as the auxiliary acceptor to further widen the spectral response range in combination with a thiophene unit as the π-bridge for the target dyes **PY-1**. Moreover, in order to further widen the absorption spectrum and enhance molar extinction coefficient (ε) of dye, a conjugated π-bridge unit cyclopentadithiophene (CPDT) was inserted between the auxiliary acceptor and thiophene for the target dyes **PY-2**. The **PY-1** and **PY-2** were synthesized by 3-bromo-1-(2-ethylhexyl)-10-(4-((2-ethylhexyl)oxy)phenyl)-1H-phenanthro [1,10,9,8cdefg]carb azole as the starting material and the general synthetic routes were depicted in Scheme 2. Firstly, we performed the well-known Buchwald coupling reaction of starting material and indoline in the presence of tri(tert-butyl)phosphine, palladium acetate and potassium tert-butoxide to yield the key intermediate **1a**. **1b** (**1a** monobromo product) with 3 equiv of bis(pinacolato)diboron in the presence of Pd(dppf)Cl_2 generated **1c**. Then, **1c** through a 2-step Suzuki-coupling reaction to obtain **1d** and **2a**. A Stille coupling reaction of **2a** with (4,4-bis(2-ethylhexyl)-4H-cyclopenta[2,1-b:3,4-b']dithiophen-2-yl)tributylstannane in the presence of Pd(PPh_3)$_2Cl_2$ was conducted to obtain **2b**. Afterwards, (5-formylthiophen-2-yl)boronic acid and **2c** (**2b** monobromo product) to generate **2d** by a Suzuki-coupling reaction. Finally, Knoevenagel condensation of compounds **1d** (**2d**) with cyanoacetic acid in the presence of piperidine was conducted to give the target compound **PY-1** (**PY-2**). Their structures were fully characterized by ^{1}H NMR, ^{13}C NMR spectroscopy and HR-MS. (see supporting information).

3.2. Optical properties of PY-1 and PY-2

The UV–vis absorption spectra of **PY-1** and **PY-2** in dichloromethane (DCM) solution were shown in Fig. 1, and the related parameters were summarized in Table 1. The dyes exhibited two major absorption bands in wavelength ranges of at 400–500 nm and 500–800 nm, respectively. Higher energy absorption band was assigned to the π-π* transition of the aromatic rings of the donor group and lower energy broad absorption band was attributable to intramolecular charge transfer (ICT) from the donor group to cyanoacrylic acid. The absorption maxima (λ_{max}) peaks of **PY-1** and **PY-2** are located at λ = 548 and 576 nm, respectively. Obviously, the introduction a conjugated π-bridge unit CPDT can red-shift the absorption band by 28 nm and enhance ε from 2.22 × 10^4 M^{-1} cm^{-1} to 4.36 × 10^4 M^{-1} cm^{-1}. So, **PY-1** and **PY-2** that hold strong light capture capability have great potentials for dye-sensitized g-C_3N_4 photocatalytic H_2 production.

3.3. Electrochemical date

To investigate the feasibility of electron injection from excited dye into the conduction band of g-C_3N_4 and dye regeneration as well as the stability of dye molecules, cyclic voltammetry (*CV*) measurements of dyes were performed in DCM with ferrocene/ferrocenium (F_c/F_c^+) as an internal reference and 0.1 M tetra-n-butylammonium hexafluorophosphate ($TBAPF_6$) as supporting electrolyte (Fig. 2), and the relevant data are listed in Table 1. The first redox potentials of **PY-1** and **PY-2** corresponding to the HOMO levels are located at + 0.79 and + 0.76 V versus NHE, respectively, which are more positive than the redox potential of the ascorbic acid (AA) electronic sacrificial agent (+ 0.14 V vs. NHE), guaranteeing ample driving force for dye regeneration. Correspondingly, the excited state potentials corresponding to the LUMO levels were calculated from equation of $E_{LUMO} = E_{HOMO} - E_{0\text{-}0}$ were -1.24 and -1.21 V vs. NHE, respectively. The $E_{0\text{-}0}$ were estimated from overlap position between absorption and fluorescence spectra for the dyes in DCM, and the corresponding data were 2.03 and 1.97 eV, respectively. It is clear that the LUMO values of the two dyes are much more negative than the CB of g-C_3N_4 (-1.12 V [43] vs. NHE), guaranteeing sufficient driving force for electron injection from excited dye molecules to CB of g-C_3N_4. Moreover, dye molecules must be stable during the redox cycles, which are generated after the electron injection from the excited dye molecule to semiconductor conduction band. This is indispensable for efficient dye molecule regeneration and achieving sustained H_2 evolution on dye-sensitized photocatalysts in an aqueous solution containing an electronic sacrificial agent. As shown in Fig. 2, the intensities of the oxidation peaks barely decreased with increasing number of scans (20 laps) for both **PY-1** and **PY-2**, which suggests that the two sensitizers maintained good stability and exhibited almost reversible behavior during the redox cycles, indicating effective dye regeneration can be achieved by accepting an electron from an electronic sacrificial agent.

3.4. Optical properties of PY-1/g-C_3N_4/Pt and PY-2/g-C_3N_4/Pt

g-C_3N_4 were prepared according to published procedures [44,45], its crystal was confirmed by X-ray diffraction (XRD) and the chemical structure of the g-C_3N_4 was further confirmed by the FTIR spectrum (Fig. S4). **PY-1**/g-C_3N_4/Pt and **PY-2**/g-C_3N_4/Pt were prepared by impregnation method, and the detailed preparation steps were shown in experimental section. The FTIR spectra of **PY-1**(**PY-2**) and **PY-1**/g-C_3N_4/Pt (**PY-2**/g-C_3N_4/Pt) were shown in Fig. 3a. Both **PY-1** and **PY-2**

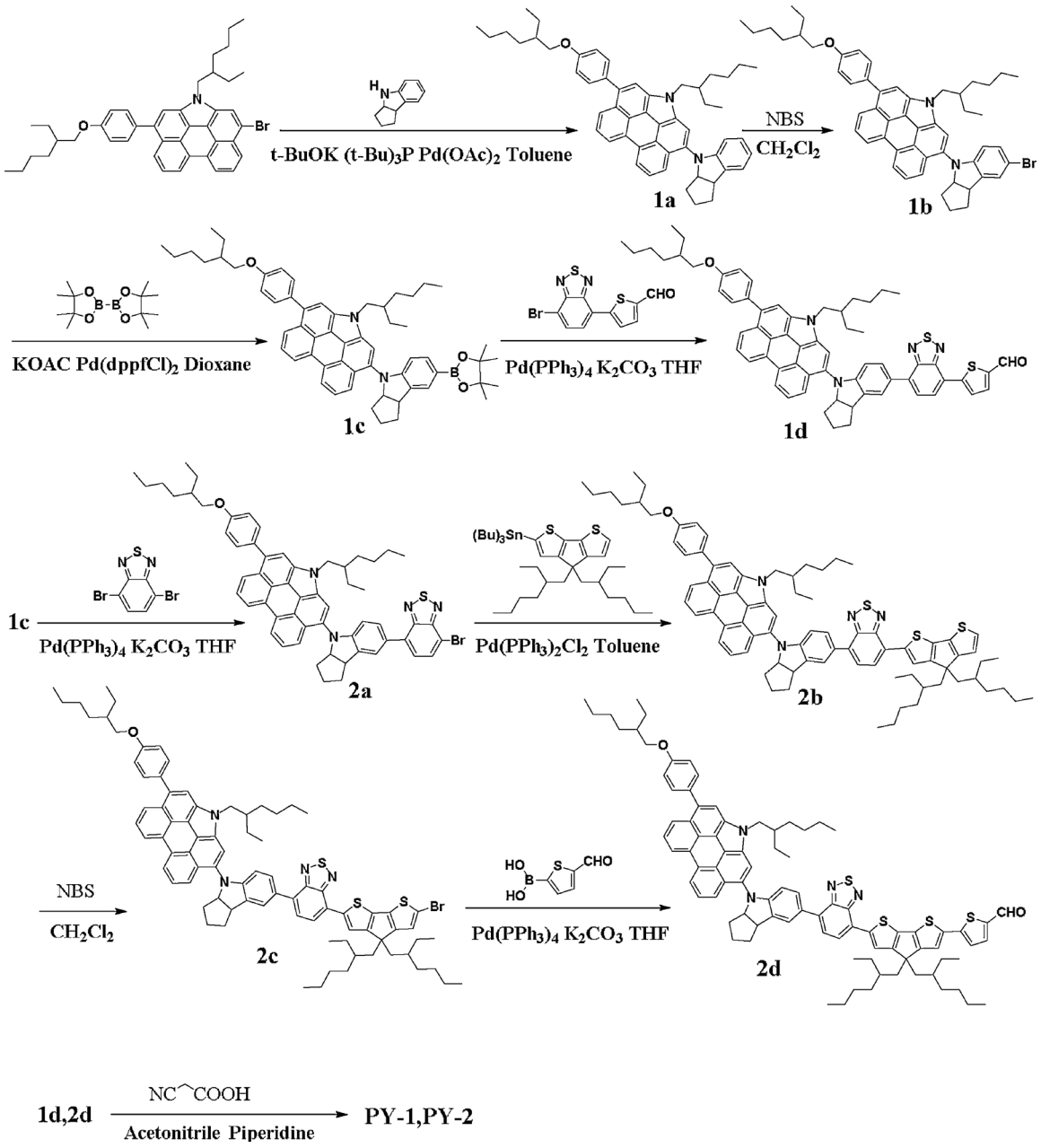

Scheme 2. General Synthetic Route of **PY-1** and **PY-2**.

showed the adsorption bands around 1600 and 2200 cm^{-1} correspond to the stretching vibration of C═O and C≡N, respectively. By contrast, an intensive absorption peaks around 3300 cm^{-1} attributable to stretching vibrations of −COOH in the dyes are extinguished after absorbing on the g-C_3N_4, and the stretching vibration of C═O in **PY-1**/g-C_3N_4/Pt (**PY-2**/g-C_3N_4/Pt) were moved to higher wavenumber compared with that of **PY-1** (**PY-2**), we guessed that the formation of amide bonds between the −COOH groups of dyes and the terminal -NH_2 groups of g-C_3N_4 during chemical adsorption process. To further confirm the above conjecture, theoretical calculations was carried out to obtain the bond length and adsorption energy (E_{ads}) (Fig. 6). The bond lengths of **PY-1**/g-C_3N_4 and **PY-2**/g-C_3N_4 were 1.42 Å and 1.43 Å, respectively, the values were consistent with the reported amide bond length [46,47]. The E_{ads} of **PY-1**/g-C_3N_4 and **PY-2**/g-C_3N_4 were 0.69 eV and 0.35 eV, respectively, indicating that the formed amide bonds were relatively stable. The Mulliken charge quantitative analysis for **PY-1**/g-C_3N_4 (**PY-2**/g-C_3N_4) further revealed that there was 0.22 e (0.25 e) transfer from **PY-1**(**PY-2**) to g-C_3N_4 (Fig. S3). Based on the above studies, it could be concluded that **PY-1**(**PY-2**) has been successfully loaded on g-C_3N_4 by forming stable amide bonds, which may serve as effective electron transfer channels to promote the charge separation and induce a synergetic effect for improved photoactivity.

The UV–vis diffuse reflectance absorption spectroscopy (*DRS*) of g-C_3N_4/ Pt, **PY-1**/g-C_3N_4/Pt and **PY-2**/g-C_3N_4/Pt were shown in Fig. 3b. The characteristic absorption edge of g-C_3N_4 is at approximately 460 nm, while the composites of **PY-1**/g-C_3N_4/Pt and **PY-2**/g-C_3N_4/Pt exhibited the entire visible-light responds (420 nm to 780 nm). Notably, **PY-1**/g-C_3N_4/Pt and **PY-2**/g-C_3N_4/Pt show obvious peak at the range of 450–600 nm, which were attributed to ICT process from the donor unit to acceptor unit in dye molecules (**PY-1** and **PY-2**). As expected, compared to the absorption of dye molecules in DCM solution (Fig. 1), **PY-1**/g-C_3N_4/Pt (**PY-2**/g-C_3N_4/Pt) had a blue shift and broadening of the absorption spectra, owing to the dye deprotonation and aggregation when adsorbed on g-C_3N_4 [57]. The results demonstrate that the

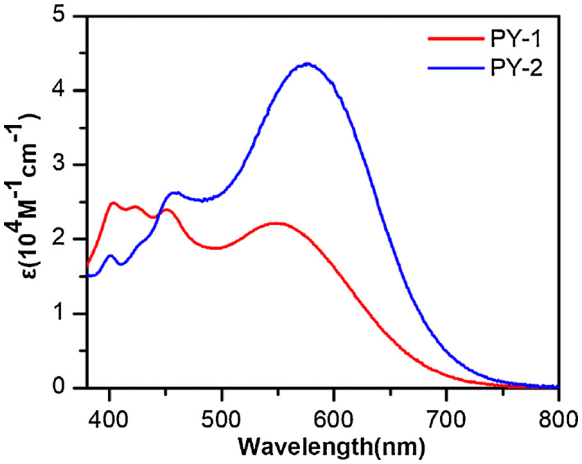

Fig. 1. UV–vis absorption spectra of dyes **PY-1** and **PY-2** in DCM solutions (3×10^{-4} M).

Table 1
Photophysical and electrochemical properties of dyes **PY-1** and **PY-2**.

Dye	λ_{max}[a] (nm)	ε (10^4 M^{-1} cm^{-1})	λ_{max}[b] (nm)	FL[c] (nm)	HOMO[d] (V)	E_{0-0}[e] (ev)	LUMO[f] (V)
PY-1	548	2.22	518	727	0.79	2.03	−1.24
PY-2	576	4.36	555	707	0.76	1.97	−1.21

[a] Absorption maximum in CH_2Cl_2 solution at RT.
[b] Absorption maximum on 4 mm transparent TiO_2 films.
[c] Emission maximum in CH_2Cl_2 solution at RT.
[d] HOMO was measured in CH_2Cl_2 with 0.1 M tetra-n-butylammonium hexafluorophosphate ($TBAPF_6$) as the supporting electrolyte (calibrated with ferrocene/ferrocenium (Fc/Fc^+) as an external reference and converted to a normal hydrogen electrode (NHE) by addition of 0.69 V).
[e] E_{0-0} was estimated from the intersection of the normalized absorption and emission spectra.
[f] LUMO was estimated by subtracting E_{0-0} from the HOMO.

application of dye-sensitized g-C_3N_4 successfully broadens the response range of g-C_3N_4 in the visible-light region, which was favorable and significant for the visible-light-driven photocatalytic H_2 production.

3.5. Photocatalytic H_2 production and stability

According to the literature [48], dye-sensitized photocatalytic H_2 production activity is usually affected by series of operating parameters such as co-catalyst Pt, the concentration of the sacrificial agent, dye-adsorbed amount and so on. Herein, we optimized the photoreaction condition before the actual photocatalytic experiments were performed, and the corresponding results were shown in Fig. S5. The results showed optimal photoreaction conditions would be: 80 mg 1 wt % Pt-loaded g-C_3N_4 sensitized with 6.2 μmol g^{-1} dye concentration, then dispersed in 50 mL of water containing 568 mM AA without adjusting the pH value. The H_2 evolution activity of g-C_3N_4/Pt, **PY-1**/g-C_3N_4/Pt and **PY-2**/g-C_3N_4/Pt under visible-light irradiation for 10 h were compiled in Table 2, and their corresponding hydrogen production-time curves were displayed in Fig. 4a. The average hydrogen evolution rates of **PY-1**/g-C_3N_4/Pt and **PY-2**/g-C_3N_4/Pt were 5508.1 μmol h^{-1} g^{-1} and 11,855.4 μmol h^{-1} g^{-1}, respectively, which were 8.98 and 19.3 times significantly higher than that of the g-C_3N_4/Pt (613.1 μmol h^{-1} g^{-1}), respectively, because of their wide visible-light response range (Fig. 3b). To further probe the effect of dye molecules on hydrogen production, the H_2 production rates of the prepared photocatalysts under various monochromatic light irradiations were also measured (λ = 420 nm, 500 nm, 550 nm, 630 nm, 700 nm) (Fig. S6). Then, according to equation 2, the wavelength-dependent AQY values were calculated based on the H_2 production rate and corresponding incident monochromatic light intensity. As shown in Fig. 4b, g-C_3N_4/Pt, **PY-1**/g-C_3N_4/Pt and **PY-2**/g-C_3N_4/Pt exhibited AQY values as the similar changing tendency as their respective DRS curves. AQY values of 18.35 (9.7), 21.27 (11.9), 27.16 (13.2), 21.06 (10.8) and 5.35% (2.52%) were obtained with **PY-2**/g-C_3N_4/Pt (**PY-1**/g-C_3N_4/Pt) under λ = 420, 500, 550, 630 and 700 nm light irradiation, respectively. These AQY values were much higher than that of g-C_3N_4/Pt, demonstrating that photocatalytic H_2 production in the range of 460–780 nm light irradiation should be mainly dominated by **PY-1** and **PY-2**. Notably, to the best of our knowledge, AQY of 27.16% at λ = 550 nm is a record value in dye-sensitized g-C_3N_4 system.

The long-term photostability of the **PY-1**/g-C_3N_4/Pt and **PY-2**/g-C_3N_4/Pt photocatalysts were tested in six consecutive runs of accumulatively 60 h irradiation with fresh AA (568 mM) solution periodically replaced in each run (Fig. 5a). After six recycles, above 85% photocatalytic activity of **PY-1**/g-C_3N_4/Pt and **PY-2**/g-C_3N_4/Pt can be maintained, implying that the photocatalysts had considerable stability and repeatability for H_2 evolution under visible-light irradiation, which was favorable and significant for practical applications in the future. In particular, *DRS* and *FTIR* of the **PY-1**/g-C_3N_4/Pt and **PY-2**/g-C_3N_4/Pt photocatalysts before and after irradiation showed no obvious signs of photodegradation (Fig. 5b and c). Furthermore, as shown in Fig. 5d, on the one hand, there is no absorption signal of **PY-1** and **PY-2** in the filtrate of the **PY-1**/g-C_3N_4/Pt and **PY-2**/g-C_3N_4/Pt suspension after irradiation, indicating that no dyes molecule desorbed from g-C_3N_4 surface and the light capture ability did not significant became weak after irradiation. On the other hand, the desorbed samples before/after irradiation which were obtained by a desorption process: photocatalysts

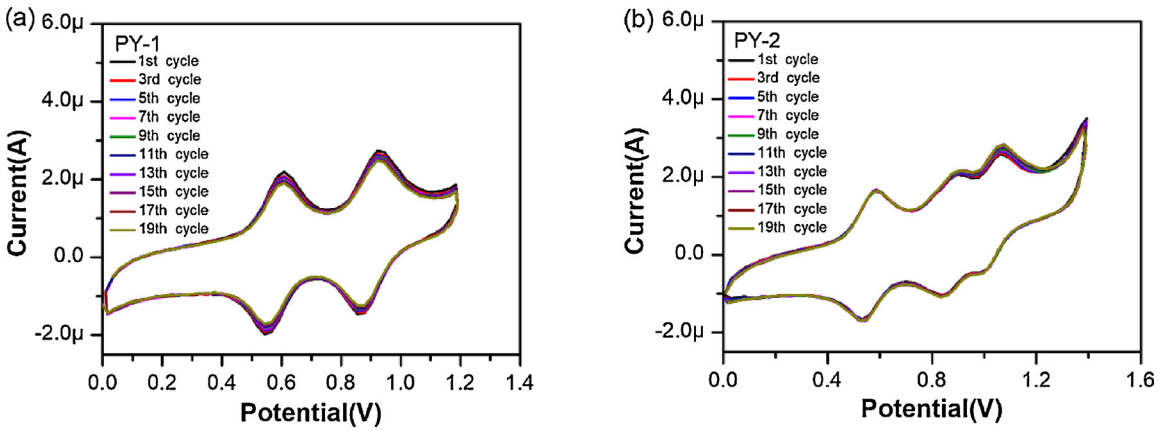

Fig. 2. CV profiles of dyes (a) **PY-1**; (b) **PY-2** in CH_2Cl_2 containing 0.1 m TBAP as a supporting electrolyte. The scan rate was 100 mV s^{-1}.

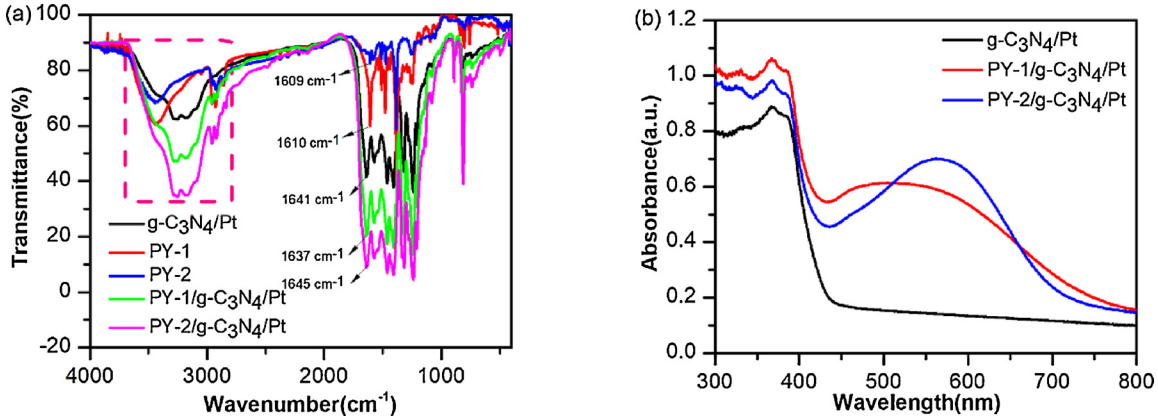

Fig. 3. (a) *FTIR* spectrum of **PY-1**, **PY-2**, **PY-1**/g-C_3N_4/Pt and **PY-2**/g-C_3N_4/Pt; (b) UV–vis diffuse reflectance spectra of g-C_3N_4/Pt, **PY-1**/g-C_3N_4/Pt and **PY-2**/g-C_3N_4/Pt.

Table 2
Photovoltaic and photocatalytic performance of dyes **PY-1** and **PY-2**.

Dye	Dye-loading (μmol/100 mg)	H_2 generation rate (μmol h^{-1} g^{-1})	TON[a]	V_{OC} (mV)	J_{SC} (mA cm^{-2})	FF[b]	PCE[c] (%)
PY-1	0.62	5508.1	18358.3	652	15.42	0.668	6.71
PY-2	0.62	11,855.4	39516.7	694	18.78	0.671	8.73

[a] TON = 2× number of evolved H_2 molecules/number of dye molecules adsorbed.
[b] FF = fill factor.
[c] PCE = power conversion efficiency. Detailed test in ESI.

were dispersed in 0.5 M NaOH in ethanol/water solution several times, and the liquid supernatant was collected. The UV–vis absorption intensity of desorbed solutions of the **PY-1**/g-C_3N_4/Pt and **PY-2**/g-C_3N_4/Pt after irradiation were just slightly less than that before irradiation (Fig. 5d), which demonstrated that no dye molecules falloff during the long-term stirring and irradiation and further explained the stability of photocatalysts under long-term irradiation.

3.6. Theoretical calculation

To obtain further insights into the molecular structure and electronic configuration of **PY-1**, **PY-2**, g-C_3N_4, **PY-1**/g-C_3N_4 and **PY-2**/g-C_3N_4, spin-unrestricted density functional theory (DFT) calculations were performed using the Gaussian 09 program package [55]. All structures were optimized without symmetry constrains and the frontier molecular orbitals were determined at the B3LYP/6-31G* level [56]. In order to simplify the calculation process without affecting the nature of key electronic structures, the long alkoxyl chains were replaced by methoxy groups. B3LYP/6-31G* wave functions of the frontier molecular orbital in **PY-1**, **PY-2**, g-C_3N_4, **PY-1**/g-C_3N_4 and **PY-2**/g-C_3N_4 were shown in Fig. 6 and Tables S3. As it can be seen, the HOMOs were mainly located on the N-annulated perylene-based donor part and the LUMOs were mainly located on the acceptor part for both **PY-1** and **PY-2**, demonstrating that both dyes have strong ICT process which can promote the photoelectron transfer. The insertion of CPDT moiety significantly extends the π-conjugation of the donor in **PY-2**, which increases the HOMO energy and facilitates its oxidation. Consequently, **PY-2** exhibits a lower HOMO to LUMO energy gap (1.89 eV) compared to **PY-1** (2.16 eV), which, in turn, corresponds well with the red shift of the absorption spectra. Moreover, the calculated relative band energy levels **PY-1**, **PY-2**, g-C_3N_4 are summarized in Fig. S1. The LUMOs level of **PY-1** and **PY-2** are -1.23 and -1.26 V vs. NHE, respectively, and their HOMOs level are 0.93 and 0.63 V vs. NHE, respectively. These results showed that both the LUMO values were more negative than that of g-C_3N_4 (-1.08 V vs. NHE), indicating that photoelectrons from **PY-1** or **PY-2** should be effectively injected into the CB of the g-C_3N_4. The two HOMO values are also more positive than that of AA (0.14 V vs. NHE), guaranteeing ample driving force for dye regeneration. Indeed, our theoretical results agree wells with the experiment. Then, **PY-1**/g-C_3N_4 and **PY-2**/g-C_3N_4 were constructed by forming an amide bond (Fig. 6). Notably, the HOMOs of **PY-1**/g-C_3N_4 and **PY-2**/g-C_3N_4 are still mainly located on the N-annulated perylene-based donor part, while the

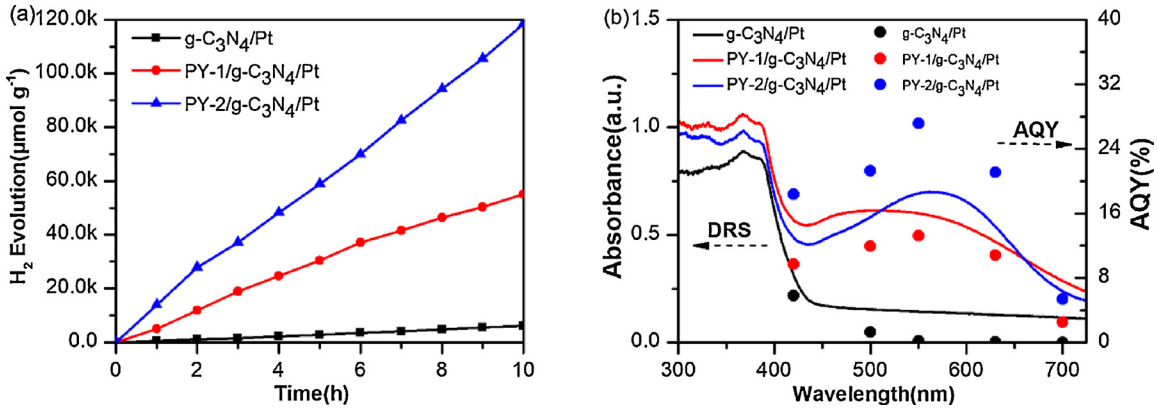

Fig. 4. (a) Photocatalytic for H_2 production over g-C_3N_4/Pt, **PY-1**/g-C_3N_4/Pt and **PY-2**/g-C_3N_4/Pt. Reaction conditions: 10 h irradiation under visible light (420 nm ≤ λ ≤ 780 nm), 80 mg photocatalyst, 50 mL water and 568 mM AA; (b) Wavelength-dependent AQY and DRS spectra of **PY-1**/g-C_3N_4/Pt and **PY-2**/g-C_3N_4/Pt under optimal photoreaction conditions (λ = 420 nm, 500 nm, 550 nm, 630 nm, 700 nm).

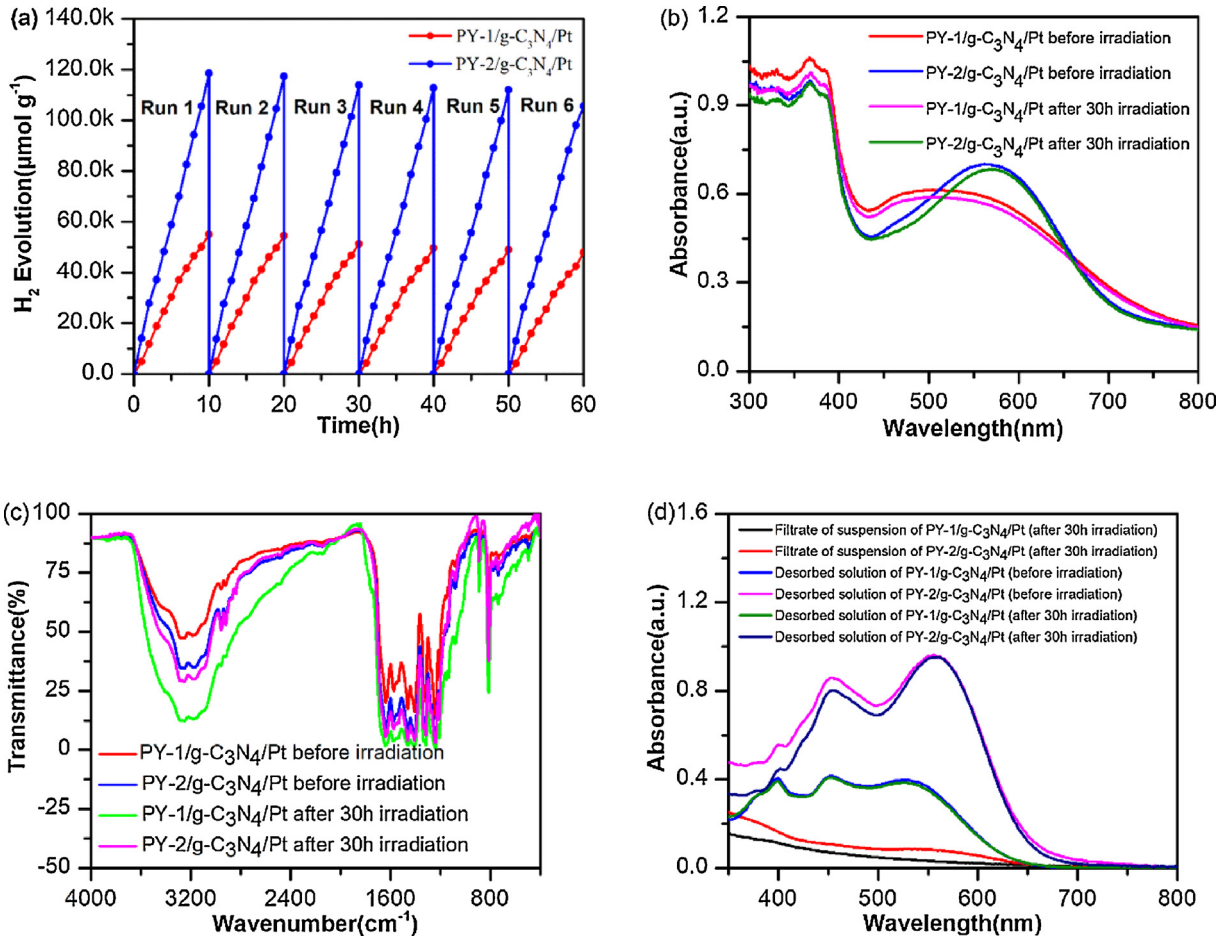

Fig. 5. (a) Photostability for H_2 production of the **PY-1**/g-C_3N_4/Pt and **PY-2**/g-C_3N_4/Pt under visible-light irradiation. Conditions: 80 mg photocatalyst, 50 mL water and 568 mM AA; (b) UV–vis diffuse reflectance spectra of **PY-1**/g-C_3N_4/Pt and **PY-2**/g-C_3N_4/Pt before and after irradiation; (c) *FTIR* spectrum of **PY-1**/g-C_3N_4/Pt and **PY-2**/g-C_3N_4/Pt before and after 30 h irradiation; (d) UV–vis spectra of the desorbed **PY-1** and **PY-2** solution and the filtrate of the **PY-1**/g-C_3N_4/Pt and **PY-2**/g-C_3N_4/Pt suspension before and after 30 h irradiation.

LUMOs are mainly located on the g-C_3N_4, demonstrating that photogenerated electrons generated in excited dyes can be easily transferred to g-C_3N_4 through the amide bond. Remarkably, they give much lower HOMO to LUMO energy gaps (**PY-1**/g-C_3N_4: Eg = 1.66 eV; **PY-2**/g-C_3N_4: Eg = 1.31 eV) compared to g-C_3N_4 (Eg = 3.63 eV). Consequently, the dye-modified g-C_3N_4 should show much broader visible-light spectrum response range, leading to much higher photocatalytic H_2 production activity than g-C_3N_4. It is also consistent with the experimental results.

3.7. Possible photocatalytic mechanism

The ultrafast electron transfer process from dye to g-C_3N_4 can be investigated by photoluminescence (*PL*) spectroscopy shown in Fig. 7a. **PY-1** and **PY-2** showed emission peaks at 727 nm and 707 nm, respectively, with excitation wavelength of 548 nm and 576 nm, which was attributed to the photogenerated carrier recombination of the sensitizers, and an obvious quenching effect can be observed with the addition of g-C_3N_4, hinting the efficient charge transfer process from excited state of **PY-1**and **PY-2** to the conduction band (CB) of g-C_3N_4 in view of fact that the absorption spectrum of g-C_3N_4 showed no overlap with the emission spectrum of the sensitizers [49]. This result is consistent with the conclusion gotten from above the possibility of thermodynamics. Furthermore, the electron injection dynamics from **PY-1** and **PY-2** and g-C_3N_4 can be further investigated by the timeresolved fluorescence spectra (*TRFS*) shown in Fig. 7b. The short fluorescence lifetime (τ_1) of **PY-1** and **PY-2** solution were 0.24 and 0.46 ns, respectively, which relates to the fast charge recombination of the excited state. Whereas the corresponding τ_1 value are prolonged to 0.36 and 0.87 ns with the addition of g-C_3N_4, respectively, which may be ascribed to the efficient electron injection from the excited **PY-1** and **PY-2** to the CB of g-C_3N_4.

In addition, linear scan voltammetry (*LSV*), transient photocurrent responses (*I-t*) and electrochemical impedance spectra (*EIS*) of g-C_3N_4 and dye-loaded g-C_3N_4 films electrode were tested using a three-electrode cell system to investigate the interfacial electron transfer kinetics. The *LSV* of g-C_3N_4 and dye-sensitized g-C_3N_4 membrane electrodes under illumination were depicted in Fig. S7a. The photocurrent density increased with applied potential from -0.4-1.2 V (vs Ag/AgCl) and reached a plateau at E > 0 V. The values were higher than the photocurrent densities under dark conditions, indicating that electrodes were all indeed photoactive. So + 0.4 V (vs Ag/ AgCl) was selected as the applied bias to record the transient photocurrent responses of the g-C_3N_4, **PY-1**/g-C_3N_4 and **PY-2**/g-C_3N_4 membrane electrodes. Fig. 7c shows *I-t* curves for all the as-prepared film electrodes with several on-off intermittent visible-light irradiation cycles. It is clear that the photocurrent exhibits good repeatability with the light off and on, and the results corresponding to their good stability of hydrogen production. The membrane electrode of **PY-2**/g-C_3N_4 showed the highest photocurrent density of 1.26 μA cm^{-2}, which is about 1.57 and 3.9 times as high as that of the membrane electrode of **PY-1**/g-C_3N_4 and bare g-C_3N_4, respectively, suggesting that more effective interfacial electron transfer from photo-excited **PY-2** to the CB of g-C_3N_4 as well as smaller recombination at its interface. Besides, *EIS* analysis is an available

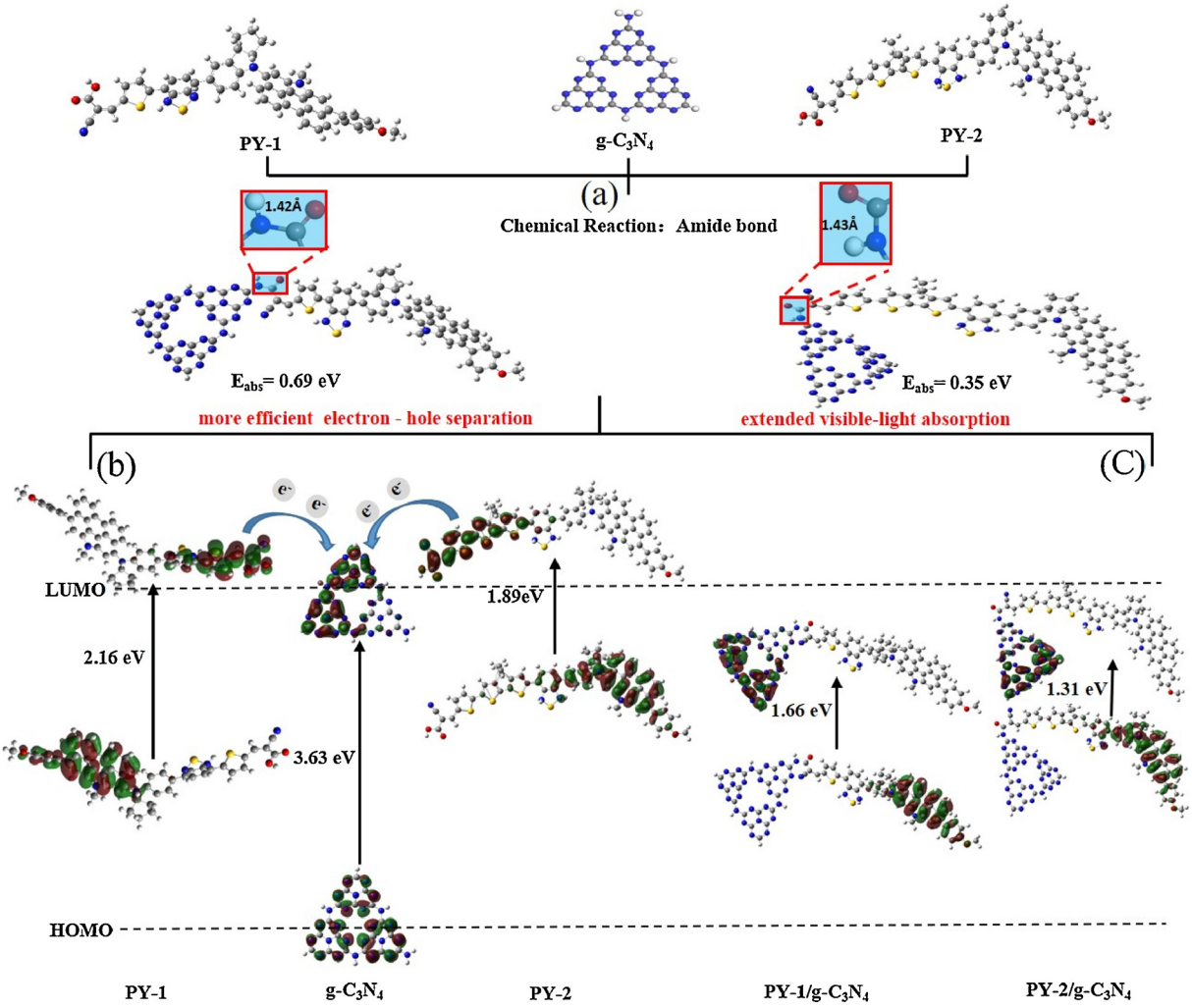

Fig. 6. The scheme of the molecular models of dye/g-C_3N_4/Pt. (a) **PY-2**/g-C_3N_4/Pt (**PY-1**/g-C_3N_4/Pt) formed between **PY-2** (**PY-1**) and g-C_3N_4 via amide bonds for efficient photocatalytic hydrogen production under visible-light irradiation; (b) The dye molecules (**PY-1** and **PY-2**) were introduced for more efficient electron-hole separation of the dye/g-C_3N_4/Pt; (c) The dye molecules (**PY-1** and **PY-2**) were introduced for reduced the bandgap and broaden the spectral response range of the dye/g-C_3N_4/Pt.

method to study the charge transfer process occurring in a three-electrode system [50,51]. Fig. 7d displays the electrochemical impedance spectroscopy (*EIS*) Nyquist plots of as-prepared membrane electrodes, which correspond to their charge transfer resistance at the sample-electrode interface. The smaller the semicircle arc is, the easier the charge transfer [52]. The **PY-2**/g-C_3N_4 membrane electrode has the smallest semicircle and **PY-1**/g-C_3N_4 membrane electrode shows a smaller semicircle than bare g-C_3N_4 membrane electrode in the middle frequency region. It is consistent with the results obtained above for *I-t* curve.

Based on all of the above experiments and analyses, a proposed mechanism of photocatalytic H_2 production over the **PY-2**/g-C_3N_4/Pt (**PY-1**/g-C_3N_4/Pt) photocatalyst under visible-light irradiation were shown in Fig. 8. Briefly, a certain amount of **PY-2** (**PY-1**) adsorbed on the g-C_3N_4 surface through forming stable amide bond which acts as an electron transfer channel, and the adsorbed **PY-2** (**PY-1**) captures a photon and produces excited state **PY-2***(**PY-1***) under visible-light irradiation, then the photogenerated electrons immediately were injected into the CB of g-C_3N_4 through the amide bond electron channel, then fast migrate to the g-C_3N_4 surface and further trapped by Pt particles for H_2 production. Simultaneously, the oxidized **PY-2** (**PY-1**) can be regenerated by accepting electrons from AA to complete the cycle.

4. Conclusions

In summary, two new NP-based organic sensitizers **PY-1** and **PY-2** were successfully synthesized and characterized for applications in dye-sensitized g-C_3N_4 for photocatalytic H_2 evolution under visible-light irradiation (420 nm $\leq \lambda \leq$ 780 nm). Notably, amide bonds were formed during dye adsorption g-C_3N_4, which act as electron transfer channels to significantly enhance interface charge transfer and separation. The H_2 production rates of the **PY-1**/g-C_3N_4/Pt and **PY-2**/g-C_3N_4/Pt were 5508.1 μmol h^{-1} g^{-1} and 11,855.4 μmol h^{-1} g^{-1}, respectively, which were 8.98 and 19.3 times higher than that of the g-C_3N_4/Pt, respectively. Importantly, an AQY of 27.16% at λ = 550 nm were achieved for **PY-2**/g-C_3N_4/Pt system, to the best of our knowledge, which is the highest AQY value so far reported among the family of dye-sensitized g-C_3N_4 photocatalysts. This might be mainly attributed to the good visible-light response and more effective interfacial electron transfer on the g-C_3N_4 surface of **PY-2**/g-C_3N_4/Pt system. In addition, **PY-1**/g-C_3N_4/Pt and **PY-2**/g-C_3N_4/Pt displayed good stability under long-term irradiation, which was favorable and significant for practical application. The present work shows that we can fine-tune the dye structure to adjust the visible-light response range of photocatalysis and improve the photocatalytic hydrogen production.

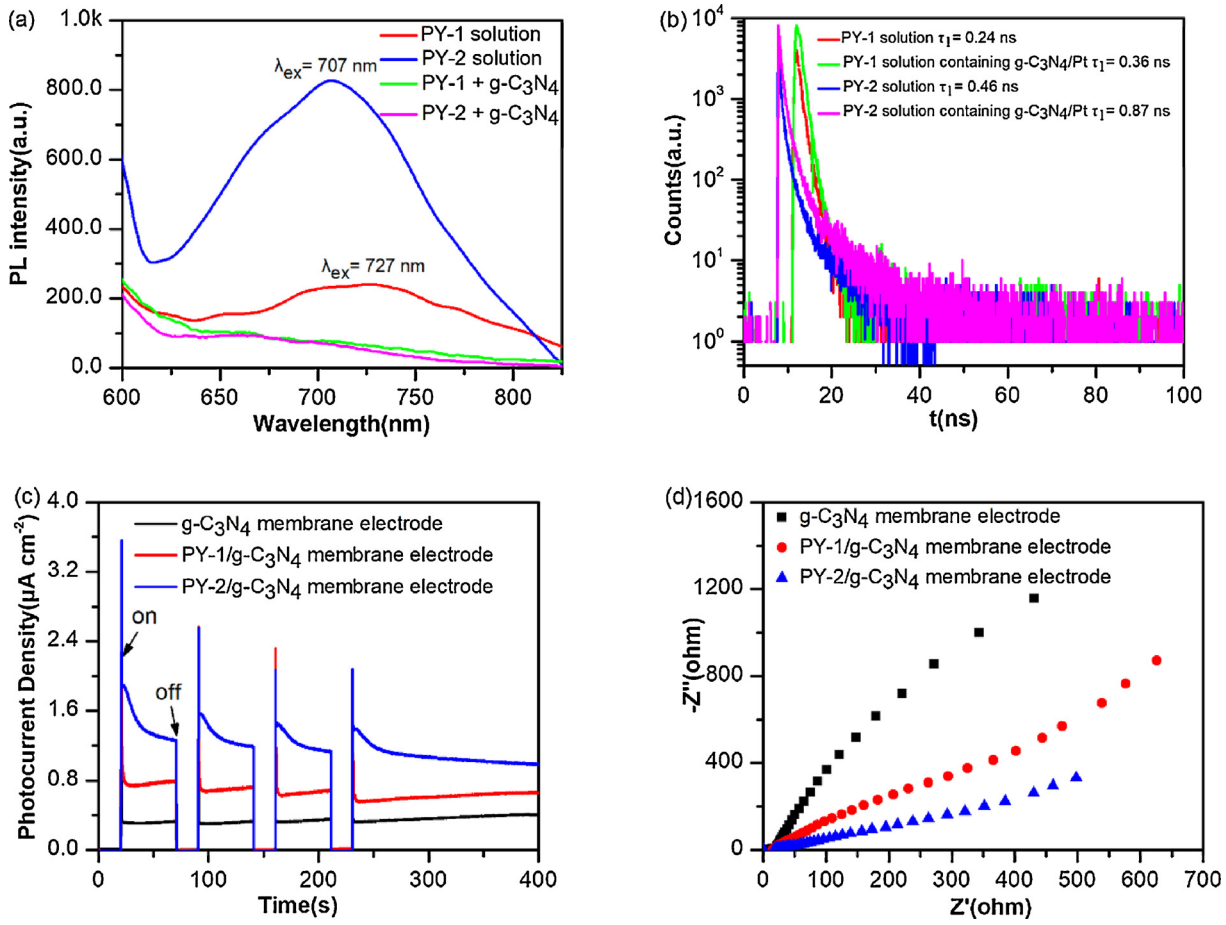

Fig. 7. (a) Photoluminescence (*PL*) spectra of the **PY-1** and **PY-2** in CH_2Cl_2 solution and the quenching effect of 0.33 g L^{-1} g-C_3N_4;(b) Time-resolved fluorescence decay curves of **PY-1** and **PY-2** solution (10 μM) with/without adding g-C_3N_4; (c) Transient current responses to on-off cycles and full time photocurrent of illumination on photoanodes under an applied bias potential of +0.4 V vs Ag/AgCl in a three-electrode PEC cell with Pt as counter electrode, operated in 0.5 M Na_2SO_4 solution; (d) *EIS* Nyquist plots of as-prepared membrane electrodes at open circuit voltage.

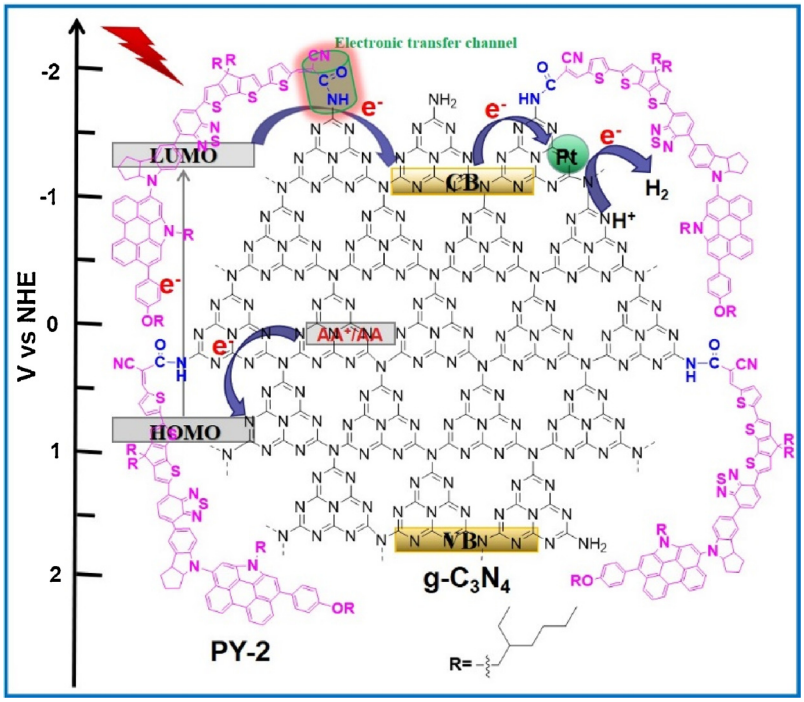

Fig. 8. Proposed photocatalytic H_2 production mechanism of the **PY-2**/g-C_3N_4/Pt.

Acknowledgements

This work was supported by the National Natural Science Foundation of China (21421004, 21572062, 21573067 and 21772040), the Fundamental Research Funds for the Central Universities (222201717003) and the Programme of Introducing Talents of Discipline to Universities (B16017).

Appendix A. Supplementary data

Supplementary material related to this article can be found, in the online version, at doi:https://doi.org/10.1016/j.apcatb.2018.05.045.

References

[1] X. Chen, S. Shen, L. Guo, S. Mao, Chem. Rev. 110 (2010) 6503–6570.
[2] Q. Xiang, J. Yu, M. Jaroniec, J. Am. Chem. Soc. 134 (2012) 6575–6578.
[3] A.J. Esswein, D.G. Nocera, Chem. Rev. 107 (2007) 4022–4047.
[4] S. Cao, J. Low, J. Yu, M. Jaroniec, Adv. Mater. 27 (2015) 2150–2176.
[5] X. Wang, G. Liu, Z. Chen, F. Li, L. Wang, G. Lu, H. Cheng, Chem. Commun. 23 (2009) 3452–3454.
[6] (a) A. Kudo, Y. Miseki, Chem. Soc. Rev. 38 (2009) 253–278;
(b) Y. Zhou, L. Zhang, J. Liu, X. Fan, B. Wang, M. Wang, W. Ren, J. Wang, M. Li, J. Shi, J. Chem. Mater. A 3 (2015) 3862–3867.
[7] B. Lin, H. Li, H. An, W. Hao, J. Wei, Y. Dai, C. Ma, G. Yang, Appl. Catal. B 220 (2018) 542–552.
[8] X. She, J. Wu, H. Xu, J. Zhong, Y. Wang, Y. Song, K. Nie, Y. Liu, Y. Yang, M. T, F. Rodrigues, R. Vajtai, J. Lou, D. Du, H. Li, P.M. Ajayan, Adv. Energy Mater. 7 (2017) 1700025–1700031.
[9] M. Watanabe, H. Hagiwara, Y.D. Ogata, A. Staykov, S.R. Bishop, N.H. Perry, Y.J. Chang, S. Ida, K.J. Tanaka, T. Ishihara, J. Mater. Chem. A 3 (2015) 21713–21721.
[10] (a) M. Watanabe, H. Hagiwara, A. Iribe, Y.D. Ogata, K. Shiomi, A. Staykov, S. Ida, K. Tanaka, T. Ishihara, J. Mater. Chem. A 2 (2014) 12952–12961;
(b) J. Willkomm, K.L. Orchard, A. Reynal, E. Pastor, J.R. Durrant, E. Reisner, Chem. Soc. Rev. 45 (2016) 9–23.
[11] (a) X. Zhang, T. Peng, S. Song, J. Mater. Chem. A 4 (2016) 2365–2402;
(b) D. Chen, K. Wang, W. Hong, R. Zong, W. Yao, Y. Zhu, Appl. Catal. B 166-167 (2015) 366–373.
[12] (a) X. Wang, K. Maeda, A. Thomas, K. Takanabe, G. Xin, J.M. Carlsson, K. Domen, M. Antonietti, Nat. Mater. 8 (2009) 76–80;
(b) P. Yang, H. Ou, Y. Fang, X. Wang, Angew. Chem. Int. Ed. 56 (2017) 3992–3996;
(c) Y. Zheng, L.H. Lin, B. Wang, X.C. Wang, Angew. Chem. Int. Ed. 54 (2015) 12868–12884.
[13] F. Liang, Y. Zhu, Appl. Catal. B. 180 (2016) 324–329.
[14] X. Hao, J. Zhou, Z. Cui, Y. Wang, Y. Wang, Z. Zou, Appl. Catal. B. 229 (2018) 41–51.
[15] B. Liu, G. Yang, B. Yang, Y. Zhao, Appl. Catal. B 198 (2016) 276–285.
[16] B. Liu, H. An, X. Yan, T. Zhang, J. Wei, G. Yang, Appl. Catal. B 210 (2017) 173–183.
[17] M. Wen, T. Xiong, Z. Zang, W. Wei, X. Tang, F. Dong, Opt. Express 24 (2016) 10205–10212.
[18] S. Zhang, J. Li, M. Zeng, J. Li, J. Xu, X. Wang, Chem. Eur. J. 20 (2014) 9805–9812.
[19] Y. Zheng, J. Liu, J. Liang, M. Jaroniec, S. Qiao, Energy Environ. Sci. 5 (2012) 6717–6731.
[20] Y. Wang, R. Shi, J. Lin, Y. Zhu, Energy Environ. Sci. 4 (2011) 2922–2929.
[21] C. Pan, J. Xu, Y. Wang, D. Li, Y. Zhu, Adv. Funct. Mater. 22 (2012) 1518–1524.
[22] (a) X. Xu, G. Liu, Int. J. Hydrogen Energy 36 (2011) 13501–13507;
(b) L. Ge, C. Han, X. Xiao, L. Guo, Int. J. Hydrogen Energy 38 (2013) 6960–6969.
[23] Y. Wang, X. Bai, C. Pan, J. He, Y. Zhu, J. Mater. Chem. 22 (2012) 11568–11573.
[24] J. Fu, B. Tian, F. Xi, X. Dong, J. Mater. Chem. A 1 (2013) 3083–3090.
[25] H. Ren, S. Jia, Y. Wu, S. Wu, T. Zhang, X. Han, Ind. Eng. Chem. Res. 53 (2014) 17645–17653.
[26] M. Tahir, C. Cao, N. Mahmood, F.K. Butt, A. Mahmood, F. Idrees, S. Hussain, M. Tanveer, Z. Ali, I. Aslam, ACS Appl. Mater. Interfaces 6 (2014) 1258–1265.
[27] X. Bai, L. Wang, R. Zong, Y. Zhu, J. Phys. Chem. C 117 (2013) 9952–9961.
[28] D. Martin, K. Qiu, S.A. Shevlin, A.D. Handoko, X. Chen, Z. Guo, J. Tang, Angew. Chem. Int. Ed. 53 (2014) 9240–9245.
[29] X. Chen, S. Shen, L. Guo, S. Mao, Chem. Rev. 110 (2010) 6503–6570.
[30] K. Takanabe, K. Kamata, X. Wang, M. Antonietti, J. Kubota, K. Domen, Phys. Chem. Chem. Phys. 12 (2010) 13020–13025.
[31] X. Zhang, U. Veikko, J. Mao, P. Cai, T. Peng, Chem. Eur. J. 18 (2012) 12103–12111.
[32] E.S. Da Silva, N.M. Moura, M. Neves, A. Coutinho, M. Prieto, C.G. Silva, J.L. Faria, Appl. Catal. B 221 (2018) 56–69.
[33] X. Zhang, T. Peng, L. Yu, R. Li, Q. Li, Z. Li, ACS Catal. 5 (2015) 504–510.
[34] Z. Ning, Y. Fu, H. Tian, Energy Environ. Sci. 3 (2010) 1170–1181.
[35] W. Jiang, H. Qian, Y. Li, Z. Wang, J. Org. Chem. 73 (2008) 7369–7372.
[36] L. Yang, Z. Zheng, Y. Li, W. Wu, H. Tian, Z. Wang, Chem. Commun. 51 (2015) 4842–4845.
[37] J. Luo, M. Xu, R. Li, K. Huang, C. Jiang, Q. Qi, W. Zeng, J. Zhang, C. Chi, P. Wang, J. Am. Chem. Soc. 136 (2014) 265–272.
[38] Z. Yao, M. Zhang, H. Wu, L. Yang, R. Li, P. Wang, J. Am. Chem. Soc. 137 (2015) 3799–3802.
[39] Y. Ren, Y. Li, S. Chen, J. Liu, J. Zhang, P. Wang, Energy Environ. Sci. 9 (2016) 1390–1399.
[40] Z. Yao, H. Wu, Y. Li, J. Wang, J. Zhang, M. Zhang, Y. Guo, P. Wang, Energy Environ. Sci. 8 (2015) 3192–3197.
[41] Z. Yao, H. Wu, Y. Ren, Y. Guo, P. Wang, Energy Environ. Sci. 8 (2015) 1438–1442.
[42] X. Zhang, L. Yu, C. Zhuang, T. Peng, R. Li, X. Li, ACS Catal. 4 (2014) 162–170.
[43] Y. Wang, J. Hong, W. Zhang, R. Xu, Catal. Sci. Technol. 3 (2013) 1703–1711.
[44] R.A. Rather, S. Singh, B. Pal, Appl. Catal. B 213 (2017) 9–17.
[45] A.J. Kirby, I.V. Komarov, K. Kowski, P. Rademacher, J. Chem. Soc. Perkin Trans. 2 (1999) 1313–1316.
[46] R. Szostak, J. Aube´, M. Szostak, Chem. Comm. 51 (2015) 6395–6398.
[47] X. Chen, S. Shen, L. Guo, S. Mao, Chem. Rev. 110 (2010) 6503–6570.
[48] X. Zhang, B. Peng, S. Zhang, T. Peng, ACS Sustain Chem. Eng. 3 (2015) 1501–1509.
[49] Y. Bu, Z. Chen, W. Li, Appl. Catal. B. 144 (2014) 622–630.
[50] M. Ye, J. Gong, Y. Lai, C. Lin, Lin Z, J. Am. Chem. Soc. 134 (2012) 15720–15723.
[51] J. Ran, J. Zhang, J. Yu, M. Jaroniec, S. Qiao, Chem. Soc. Rev. 43 (2014) 7787–7792.
[52] F. Yu, S. Cui, X. Li, Y. Peng, Y. Yu, K. Yun, S.C. Zhang, J. Li, J. Liu, J. Hua, Dyes Pigm. 139 (2017) 7–18.
[53] X. Zhang, Y. Xu, F. Giordano, M. Schreier, N. Pellet, Y. Hu, C.Y. Yi, N. Robertson, J. Hua, S.M. Zakeeruddin, H. Tian, M. Gratzel, J. Am. Chem. Soc. 138 (2016) 10742–10745.
[54] M. J. Frisch, G.Inc, Wallingford CT, 2009.
[55] W.J. Hehre, R. Ditchfield, J.A. Pople, J. Chem. Phys. 56 (1972) 2257–2261.
[56] J. Chen, C.L. Dong, D. Zhao, Y.C. Huang, X.X. Wang, L. Samad, L.N. Dang, M. Shearer, S.H. Shen, L.J. Guo, Adv. Mater. 29 (2017) 1606198–1606208.
[57] Q. Chai, W. Li, J. Liu, Z. Geng, H. Tian, W. Zhu, Sci. Rep. 5 (2015) 11330–11340.